Icarus 427 (2025) 116376

Contents lists available at ScienceDirect

Icarus

journal homepage: www.elsevier.com/locate/icarus

Research Paper

Lifetime, size and emission of laser-induced plasmas for in-situ laser-induced breakdown spectroscopy on Earth, Mars and Moon

Fabian Seel [a,b,*], Susanne Schröder [a], Elise Clavé [a], Enrico Dietz [a], Peder Bagge Hansen [a], Kristin Rammelkamp [a], Heinz-Wilhelm Hübers [a,b]

[a] Institute of Optical Sensor Systems, German Aerospace Center (DLR), Rutherfordstraße 2, Berlin, 12489, Germany
[b] Department of Physics, Humboldt-Universität zu Berlin, Newtonstraße 15, Berlin, 12489, Germany

ARTICLE INFO

Keywords:
LIBS
LIP
Plasma imaging
Plasma size
Plasma dynamics
Plasma emission
Earth
Mars
Moon
Vacuum

ABSTRACT

The spectroscopic technique of laser-induced breakdown spectroscopy (LIBS) is a powerful method to perform rapid chemical analysis of geologic samples with short measurement times and no need for sample preparation. After the ChemCam instrument aboard NASA's MSL rover proved its suitability for space missions that explore planetary surfaces in 2012, the interest in LIBS instruments as payloads has grown and several subsequent missions have successfully used this technique since. The characteristics of a LIBS plasma depend on experimental and environmental parameters as well as on sample properties, including atmospheric conditions, laser irradiance and sample lithology. Consequently, LIBS instruments need to be designed and optimized specifically for each use case to maximize their science output. To aid in the development of new LIBS instruments for space exploration, we investigate the influence of atmospheric conditions, laser irradiance and sample lithology on the lifetime, size and emission of laser-induced plasmas. In our measurements, we use a plasma imaging setup with high temporal resolution of down to 2 ns to investigate the evolution of the plasma from its ignition to its decay. We present a comparable data set recorded at terrestrial, Martian and airless atmospheric conditions, covering irradiances between 0.79 GW/mm^2 and 1.43 GW/mm^2 and samples with diverse properties, namely basalt and soapstone, as well as the lunar regolith simulants LHS-1 and LMS-1. Our measurements show the strong influence of atmospheric conditions on the plasma size and emission, while the lithologies and laser irradiances covered in this work play a minor role. This shows that instruments designed to work at certain atmospheric conditions can be used for a range of laser parameters and sample properties. Furthermore, we demonstrate that the decay of the plasma emission and the expansion of the plasma plume parallel to the sample surface can be described well by a power law and a drag model, respectively.

1. Introduction

When NASA's Mars Science Laboratory (MSL) rover Curiosity landed on Mars in August 2012, it delivered the first operational laser-induced breakdown spectroscopy (LIBS) instrument for planetary in-situ analysis to Mars (Maurice et al., 2012; Wiens et al., 2012; Maurice et al., 2016) and has since been collecting data on the Martian surface geochemistry. LIBS is an elemental analysis technique that allows rapid collection of data, can be used without prior preparation of the sample, and requires only optical access to the sample, thus enabling remote measurements at up to a few meters distance with current systems (Knight et al., 2000; Maurice et al., 2012). Since ChemCam proved that LIBS is well suited for in-situ analysis in Solar System exploration, particularly for the analysis of rocks and soils on Mars, several subsequent missions also included LIBS instruments.

In 2021, the Mars 2020 rover Perseverance carried the second LIBS instrument to the Martian surface (Maurice et al., 2021; Wiens et al., 2021) and a few months later, the third LIBS instrument on Mars became operational aboard the Zhurong rover (Wan, 2021). The first functional LIBS instrument on the Moon was deployed two years later in 2023 as a payload of the rover Pragyan (Laxmiprasad et al., 2020).

To perform a LIBS measurement, a pulsed laser beam is focused on the sample surface, where the intense radiation evaporates some of the sample material and turns it into a plasma. A spectral analysis of the plasma emission can then reveal the constituents of the plasma and therefore the elemental composition of the sample.

In order to acquire high quality LIBS data, the LIBS instrument has to be designed for the specific scenario it is used in, since the plasma

* Correspondence to: Mister Fabian Seel, German Aerospace Center DLR, Institute of Optical Sensor Systems, Department In-Situ Sensing, Rutherfordstraße 2, 12489, Berlin, Germany.
E-mail address: fabian.seel@dlr.de (F. Seel).

https://doi.org/10.1016/j.icarus.2024.116376
Received 14 September 2024; Received in revised form 4 November 2024; Accepted 12 November 2024
Available online 20 November 2024

properties and consequently the characteristic emission from plasma species are strongly dependent on experimental and environmental parameters. This is particularly important for applications in space exploration where experimental conditions cannot be controlled like they can in laboratory environments on Earth. Parameters to consider include the laser irradiance and the atmospheric composition and pressure (Knight et al., 2000; Schröder et al., 2019). Additionally, the sample's composition and its physical properties can affect the laser-induced plasma (LIP). In particular, these parameters can influence the lifetime, size and emission of the laser-induced plasma, leading to different instrument requirements regarding the instrument's sensitivity, field of view, depth of field, focusing ability, and the timescales it needs to operate in Knight et al. (2000), Schröder et al. (2019).

Since experimental and environmental parameters for in-situ research on planetary bodies vary significantly, the LIBS instrument design has to be adapted for each mission scenario not only to be operational in the respective ambient conditions but also to best meet the mission's science goals. Specifically, this means adapting the instrument's field of view for the plasma's size, and choosing a sensor in accordance with the plasma's emission and lifetime to maximize the desired signal and minimize the impact of noise. Currently, several lander missions for Solar System exploration are in preparation (Lorenz et al., 2018), with a particular interest in moon landers (Carpenter et al., 2012; Ennio-Smith, 2022). This also creates a prospect of new LIBS instruments for in-situ geochemical analysis and other applications such as in the context of in-situ research utilization (ISRU) (Rammelkamp et al., 2024).

Studies on LIBS for in-situ research on planetary surfaces were first presented in 1992 when sufficiently capable lasers were available (Kane and Cremers, 1992b,a). These and subsequent works include studies on the influence of atmospheric pressure on the size of the laser-induced plasma (LIP) and its spectral characteristics, covering a pressure range from terrestrial atmospheric pressure down to vacuum (Knight et al., 2000; Lasue et al., 2012). The prospect of a LIBS instrument for the harsh Venusian environment with ambient pressures of 9.1 MPa was also investigated (Arp et al., 2004).

In this work, we expand on previous studies by examining the spatiotemporal evolution of the plasma emission at different atmospheric conditions, different laser irradiances and for different sample lithologies, with the goal to provide insights that can guide the optical design of future LIBS systems for extraterrestrial low pressure environments. We cover three atmospheric conditions — representing Earth for reference, Mars and airless planetary bodies — and three different laser energies — 11.86 mJ, 8.75 mJ and 6.56 mJ — that are typical for LIBS instruments employed in planetary exploration. To investigate the influence of different lithologies that can be expected in different planetary environments, we present data from four samples that cover two types of lunar regolith analogue (LMS-1 and LHS-1), a metamorphic rock (soapstone) and an igneous rock (basalt).

2. Background

The evolution of LIPs begins with the ablation process, where the sample surface is exposed to intense radiation from a pulsed laser. For space instruments, infrared laser pulses with pulse durations between 3 ns and 7 ns have been used so far (Maurice et al., 2021, 2012; Laxmiprasad et al., 2020; Xu et al., 2021). Exposing the sample surface to intense laser radiation leads to heating of the target material. The efficiency of this process depends on the material's absorption length at the laser radiation's wavelength and the thermal diffusion distance. These sample properties vary with the sample's temperature, so that the temporal and spatial profile of the irradiating laser pulse that heats the sample is also relevant to the history of the evaporation process (Singh et al., 1990). In addition to thermal evaporation, non-thermal ablation can also occur at high laser-irradiances like those used for current LIBS instruments for solar-system exploration and consequently, the solid's electronic structure also influences the ablation process (Singh and Thakur, 2020; Keldysh, 2023; Bäuerle, 2000). For the duration of the laser pulse, a combination of thermal and non-thermal ablation mechanisms leads to the generation of a vapor of sample material above the sample surface. The vapor temperature is sufficiently high so that there are always free electrons that can absorb laser energy via free-free transitions in collisions with atoms and ions through inverse bremsstrahlung radiation, further increasing the vapor temperature and ionization (Noll, 2012; Singh et al., 1990; Bogaerts et al., 2003; Autrique and Alexiades, 2014; Autrique et al., 2013a). For high irradiances, multiphoton absorption can contribute to the ionization process (Autrique et al., 2013b). All these mechanisms lead to the generation of the plasma plume. When the plasma becomes dense, increased absorption of the laser radiation within the plasma can occur and shield the sample (Autrique et al., 2013b; Radziemski and Cremers, 1989). The strength of this shielding effect depends on the plasma's absorption coefficient at the laser's wavelength, which is influenced by the irradiance of the incident laser beam (Autrique et al., 2013b). Typically, higher laser irradiances lead to a stronger shielding effect (Singh and Thakur, 2020; Mao and Russo, 1996). Furthermore, the laser wavelength influences the absorption processes, as multiphoton absorption decreases for longer wavelengths, whereas inverse bremsstrahlung absorption increases with longer wavelengths (Autrique et al., 2013a; Radziemski and Cremers, 1989). At lower ambient pressures like those on Mars, plasma shielding is reduced due to the faster plasma expansion and the accompanying faster decrease in number densities of the absorbing species (Knight et al., 2000).

The initial plasma expansion during the laser pulse was hypothesized to proceed isothermally in vacuum, with the processes of laser absorption in the plasma and evaporation rate from the target controlling the isothermal plasma temperature (Krokhin, 1965; Caruso and Gratton, 1968). Simulations employing an isothermal expansion for the duration of the laser pulse yield variable agreement with experimental data (Harilal et al., 2011; Liu et al., 2019; Murakami et al., 2005). For the initial expansion with atmospheric background pressure, the spatially averaged electron and ion temperatures in the plasma were shown to change and not equilibrate within the duration of the laser pulse in simulations (Autrique et al., 2013b).

After the laser pulse has ended, most of the plasma plume's energy is kinetic and the plasma continues to expand (Arnold et al., 1999; Harilal et al., 2003). During the expansion and cooling of the plasma, some internal energy is lost to the surroundings through radiative processes, while some is regained through the recombination and deexcitation of plasma species. For vacuum, this expansion process can be assumed to proceed adiabatically, as energy losses to the surroundings due to mechanisms such as radiation, thermal conduction and diffusion can be neglected (Singh and Narayan, 1990; Itina et al., 2002; Dyer et al., 1990). The acceleration of each plasma species depends on its respective mass, the plasma temperature and the plasma dimensions, with the shortest dimensions leading to the fastest acceleration. In a model where the plasma is initially a thin layer above the sample surface, this leads to the characteristic cone shape of plasma ablation processes in vacuum (Singh et al., 1990).

When the LIP is ignited inside an atmosphere, the expansion proceeds until a pressure equilibrium with the surroundings is reached (Hermann et al., 2018). The maximum plume size was described using an adiabatic model in Harilal et al. (2003), yielding reasonable agreement with experimental data. At pressures between about 10 Pa and 100 Pa, neither effects leading to the compression of the plume and the ambient gas, nor diffusion can be neglected, so that this regime cannot be described using an adiabatic model and mass and energy exchange with the ambient gas need to be considered (Itina et al., 2002).

The pressure of a LIP depends on its temperature and number densities and consequently, a denser and hotter LIP will expand faster. A higher plasma temperature also leads to an increase in plasma emission. Line emission is increased due to a higher population density of ionic

and atomic excited states, and continuum radiation is increased due to a higher degree of ionization, which leads to stronger recombination radiation and bremsstrahlung radiation. Inelastic collisions between particles of the plasma and the atmosphere in the plasma's leading layer can lead to energy loss and cooling in the plasma periphery (Hermann et al., 2018; Vogt et al., 2022). For this reason, argon is often employed in laboratory studies, since the high excitation energies of inert gasses favor elastic collisions. When the pressure of the plume approaches the pressure of the surroundings, diffusion between the plume and the ambient atmosphere becomes relevant, contributing to the cooling of the plasma plume (Hermann et al., 2018).

Phenomenologically, the expansion of LIPs in an atmosphere has been described previously using a drag model that assumes a drag force proportional to the expansion velocity (Geohegan, 1992).

$$r(t) = r_r(1 - e^{-\frac{t}{\tau}}) \quad (1)$$

Collisions with the ambient gas slow the plasma expansion down within the characteristic time scale τ until it comes to rest at a distance r_r from the sample surface. The drag model shows reasonable agreement with experimental data for different atmospheric compositions and a wide range of background pressures (Gonzalo et al., 1997; Geohegan, 1992; Harilal et al., 2003, 2012; Farid et al., 2013). Depending on the properties of the ablating laser pulse, the sample and the ambient gas, the characteristic time varies. Gonzalo et al. reported characteristic time scales of 2.2 µs and 1.5 µs for a plasma expanding into an oxygen atmosphere at 10 Pa and 100 Pa, respectively (Gonzalo et al., 1997). Seel et al. determined τ in a CO_2 dominated atmosphere at 1000 Pa to be about 110 ns (Seel et al., 2023). For a wide range of air pressures between 133 Pa and 101 kPa, Farid et al. found characteristic time scales between about 260 ns and 320 ns (Farid et al., 2013).

The practical effects of the ambient atmospheric conditions on LIBS data were analyzed, among others, by Knight et al. using a 10 ns laser emitting at 1064 nm with pulse energies of 80 mJ to 100 mJ (Knight et al., 2000). Using long integration times of 20 µs, they found that, starting at 1 Pa, the signal from line emission increases with pressure until it peaks at around 5 kPa. A further increase in pressure to about 80 kPa resulted in a reduction of the line emission signal. The background signal from continuum radiation, however, increased monotonically with increasing ambient pressure. They explained the initial signal increase by stronger plasma excitation through collisions in the confined plasma at lower pressures and the subsequent signal decrease by reduced ablation through plasma shielding, which also leads to a stronger background signal. At terrestrial atmospheric conditions, plasma emission can typically be detected for several tens of microseconds, though the exact times depend on the specific parameters of the experiment, including the ablating laser and the detection system (Cremers and Radziemski, 2013; Fisher et al., 2001).

With an atmospheric pressure of about 700 Pa at the landing site of the Mars 2020 rover, the ambient pressure on the surface of Mars is sufficiently high to provide good plasma confinement, while effects from plasma shielding are relatively weak so that the ablation rates are high (Harri et al., 2024; Knight et al., 2000). This makes Martian atmospheric conditions close to ideal for LIBS analyses with intense characteristic emission that is relatively long-lived with a lifetime on the order of some microseconds (Brennetot et al., 2003; Sallé et al., 2005; Vogt et al., 2022; Seel et al., 2023). When a LIP is ignited without a surrounding atmosphere, its lifetime can be expected to be on the order of some hundred nanoseconds (Gornushkin et al., 2005).

3. Experimental setup

To investigate the lifetime, size and emission of LIPs, we use an imaging setup that allows to capture images of the expanding plasma with a temporal resolution of down to 2 ns using an ICCD sensor. The setup as used here has a field of view of about 3.0 mm and is most sensitive between about 300 nm and 900 nm, which is a typical wavelength range for LIBS instruments (Vogt, 2020). A sketch of the experimental setup is shown in Fig. 1 and a detailed description can be found in Vogt (2020). The plasma is ignited inside a vacuum chamber that can be evacuated and filled with gas to experimentally simulate the atmospheric environment of other planetary bodies with low pressures. Measurements at terrestrial conditions were performed in the laboratory ambient atmosphere. Martian atmospheric conditions were simulated using a gas mixture composed of 95.55 vol% CO_2, 2.70 vol% N_2, 1.60 vol% Ar and 0.15 vol% O_2 at a pressure of (700±40) Pa. Conditions on airless bodies were simulated by keeping the vacuum pumps running during the measurement, evacuating the chamber to less than 0.3 Pa. While this pressure is orders of magnitude larger than the surface pressure on the Moon, no significant changes to the plasma dynamics are expected below about 1 Pa, as the mean free path of the ambient atmosphere approaches the size of the plasma (Knight et al., 2000; Heiken et al., 1991).

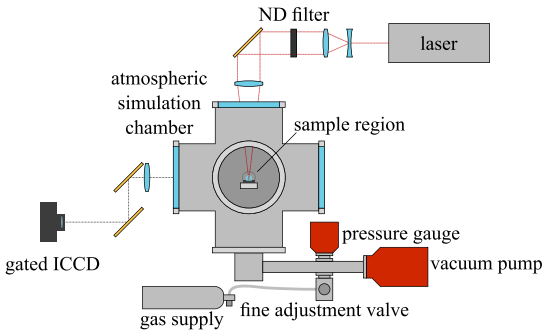

Fig. 1. Overview of the experimental setup. The laser that is used to ignite the plasma inside the simulation chamber enters from the top and can be attenuated using absorptive neutral density (ND) filters. The chamber can be evacuated and filled with a gas to simulate Martian atmospheric conditions. The plasma imaging system observes the plasma plume from the side.

To induce the plasma, a Nd:YAG laser with a FWHM pulse duration of 8.1 ns emitting at its fundamental 1064 nm mode was used. For the present study, the laser pulse energy E_L was varied between 11.86 mJ, 8.75 mJ and 6.56 mJ using neutral density filters as shown in Fig. 1. The energies were measured inside the simulation chamber from the average of 50 pulses with a standard deviation of less than 0.10 mJ in a procedure separate from the acquisition of the plasma images.

After passing the filter section, the laser is focused onto the sample surface through a movable lens with a focal length of 150 mm. A measurement of the focused laser spot is shown in the upper panel of Fig. 2. The lower panel shows the beam profile cross section in two perpendicular axes parallel to the pixel grid that cross the beam profile's centroid. To compute the beam diameter, we use the area around the beam centroid that encloses 86 % of the total laser irradiance, resulting in beam diameters of $D86_x = (33.6 \pm 2.2)$ µm in the horizontal axis and $D86_y = (33.4 \pm 2.2)$ µm in the vertical axis. These diameters are represented by the ellipse in the upper panel. The errors are estimated to be half the size of the beam profiler's pixel pitch of 4.4 µm. From the beam shape, pulse energy and pulse duration, the spatial and temporal average irradiance within the $D86$ area is computed to be (1.43 ± 0.14) GW/mm^2, (1.05 ± 0.10) GW/mm^2 and (0.79 ± 0.08) GW/mm^2, respectively.

4. Samples

The samples used in this study are shown in Fig. 3. They were selected to represent a variety of sample properties that are relevant to planetary exploration. Compacted lunar regolith is represented by Lunar Highlands Simulant (LHS-1) and Lunar Mare Simulant (LMS-1) powder from Exolith that was pressed into pellets of 13 mm diameter with a pressure of about 370 MPa. According to the manufacturer,

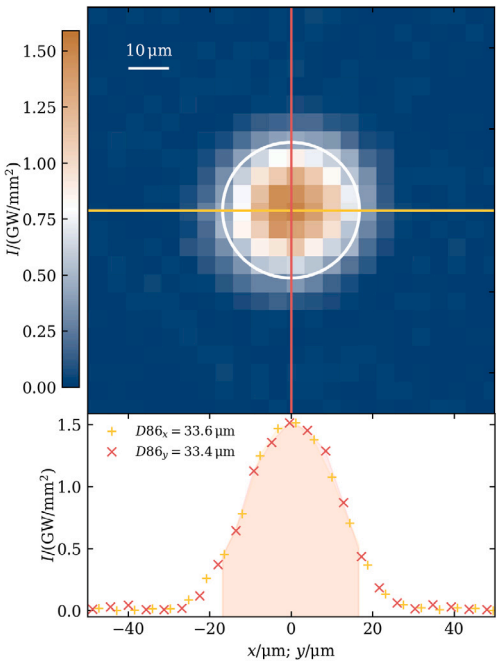

Fig. 2. Beam profile at the laser's beam waist. The top panel shows a section normal to the beam direction. The colored lines cross at the beam's centroid and the profiles along these lines are shown in the lower panel. The beam diameter according to the $D86$ criterion is marked in the top panel with a white ellipse and with a shaded area in the bottom panel. The profile was recorded from a strongly attenuated beam and the shown irradiances were extrapolated from measurements of the pulse energy. Here, the irradiance values correspond to the highest laser energy used in this study of 11.86 mJ.

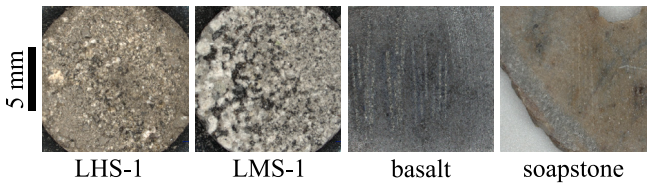

Fig. 3. Overview of the samples used for this study, covering two types of compacted regolith with LHS-1 and LMS-1, an igneous rock with basalt, and a metamorphic rock with soapstone.

LHS-1 contains 32.8 wt % bronzite, 32.0 wt % glass-rich basalt, 19.8 wt % anorthosite, 11.1 wt % olivine and 4.3 wt % ilmenite, and the LMS-1 sample contains 74.4 wt % anorthosite, 24.7 wt % glass-rich basalt, 0.4 wt % ilmenite, 0.3 wt % bronzite and 0.2 wt % olivine. The basalt and soapstone samples were cut from rocks, representing a rather hard igneous rock and a very soft metamorphic rock, respectively. For these samples, no quantitative elemental composition is available, however, LIBS spectra show emissions of all major rock forming elements, in particular strong Ca, Fe, and Ti emissions for basalt and strong Mg and Si emissions for soapstone, which is in agreement with the expected composition of samples of such rock types.

5. Methodology

5.1. Data acquisition

Each plasma image was obtained from an individual LIP. To avoid effects from cratering, the laser beam was moved across the surface during data acquisition in a direction parallel to the line of sight of the plasma imaging system. Data was acquired with a repetition rate of 2 Hz. To generate the time series shown in this work, the delay time of the ICCD gate t_d was varied between 0 ns and 10 µs after plasma ignition for terrestrial atmospheric conditions, between 0 ns and 3 µs for Martian atmospheric conditions and between 0 ns and 100 ns for airless conditions. The time $t_d = 0$ ns was determined experimentally by identifying the delay settings where the first plasma signal could be observed at terrestrial atmospheric conditions and confirmed by direct observation of the laser pulse using a frequency-doubling crystal. From our observations, we assume the error of the noted delay times to be on the order of 2 ns, corresponding to the gate width used in identifying $t_d = 0$ ns. To account for varying emission of the plasma, the gate time t_g of the ICCD was increased for increasing step sizes at longer delay times, while the gain setting was kept the same for all measurements. We used a very low gain setting to avoid saturation for strong plasma emission. It should be noted that the choice of a low gain influences the time until which plasma emission can be detected, so that other studies where different experimental settings were used may find a significant plasma emission and longer delay times than in the presented data. For most measurements, the gate time was set to 20 % of the step size. The stepsizes used are 1 ns, 10 ns, 100 ns and 1000 ns. Only for the measurements at airless conditions, the gate time was kept at 2 ns even for the step size of 1 ns, as this gate time is the lower temporal resolution limit of the plasma imaging system. The timescales covered at the different atmospheric conditions are illustrated in Fig. 4.

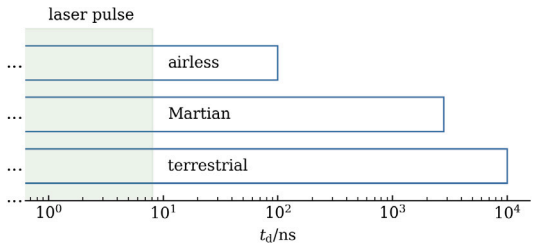

Fig. 4. Overview of the timescales covered in the plasma images for each atmospheric condition. Starting at the time of plasma ignition, the measurements cover ICCD delay times of 100 ns, 3 µs and 10 µs for airless, Martian and terrestrial atmospheric conditions, respectively. The shaded area marks the duration of the laser pulse of 8.1 ns.

Since the emitting region of the plasma at reduced ambient pressure can be larger than the plasma imaging system's field of view of about 3.0 mm, two plasma images were taken at different heights above the sample surface for measurements performed at Martian atmospheric conditions. These measurements were separated by 1.75 mm and stitched together before applying the data processing procedure described below. Since each plasma image was recorded from a separate LIP and occasionally there are some fluctuations in the exact size of the plasma and its expansion dynamics, artifacts from the stitching procedure are visible in some measurements. While we assume errors from this procedure to be small due to the generally good repeatability of the measurements, it should be mentioned that measurements using the LHS-1 and LMS-1 pressed samples were found to vary more than measurements using the rock samples. Stitched measurements are seen in Figs. 7 and 9 and all analyzed images are provided in the supplementary material. The stitching line in the presented data is located about 1.8 mm above the sample surface.

5.2. Data processing

For each plasma image, a dark image was subtracted that was recorded before each measurement with new gate settings. All plasma images were processed by first applying a uniform filter of size 8 px or about 120 µm to reduce the noise level. During data evaluation, we noticed an offset of the noise floor that increased over the course of a measurement, even though a dark measurement was subtracted. We attribute this observation to a warming of the ICCD sensor. To remove the influence of the increased noise floor, an area of the images without any signal from the plasma was identified, from where the mean signal

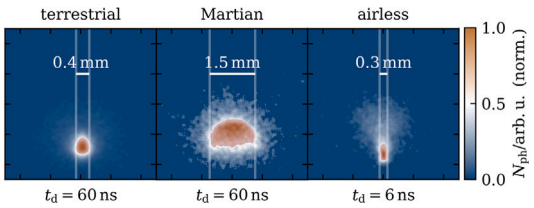

Fig. 5. Illustration of the computation method for the plasma size. The area shaded in red marks the area that is above the half maximum value and the vertical lines show the extent of the plasma parallel to the sample surface as used for the analysis. (For interpretation of the references to color in this figure legend, the reader is referred to the web version of this article.)

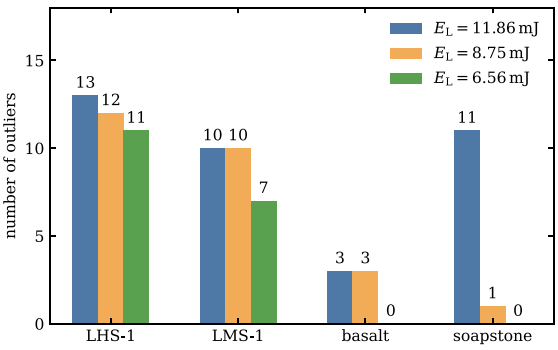

Fig. 6. Number of detected outliers at terrestrial atmospheric conditions for all samples and laser energies. The outliers are likely a result of a debris cloud of small particles that remain over the sample for at least 10 s. LHS-1 and LMS-1 are pressed from pellets and contain particles with a diameter of 1 µm or less. Soapstone was measured after the two pellet samples so that the number of outliers for soapstone could be increased due to residual debris cloud from the previous measurements.

was calculated and subtracted for each image. These processing steps are the basis for all subsequent analysis and common to all presented data products.

All data processing was done in Python, using custom libraries based on the SciPy and NumPy libraries (Virtanen et al., 2020; Harris et al., 2020).

5.2.1. Plasma size

To compute the size of the plasma, we first identified the region where the signal was above half the maximum value. For this step to work reliably with data that has low signal at late delay times, another smoothing step using a uniform filter of size 8 px or about 120 µm was required. We verified that this step does not impact the computed size of the plasma significantly. Upon identifying the region of half maximum, the full width at half maximum $FWHM_h$ was computed from the largest extent of the plasma parallel to the sample surface, as illustrated in Fig. 5. It should be noted that other methods to compute the size of the plasma from these data can lead to very different values. For example, a constant threshold signal could be used, which would lead to a decreasing plasma size as the plasma decays after expansion. We chose a normalized method that describes the plasma size from which most of the plasma signal is emitted for any given delay time, since this is relevant information when designing the field of view of LIBS instrumentation. Furthermore, the choice of defining the plasma size as the width of the plasma plume parallel to the sample surface was motivated by the typical co-linear design of LIBS instruments in space exploration, where the irradiating laser and the spectroscopic beam path share the same aperture. Knowledge of the plasma width is beneficial to inform the design of the field of view of LIBS instruments.

For better visibility, the plasma images shown here have a noise gate filter applied that sets the signal in areas without plasma emission to zero. This processing step was only applied for visualization purposes and was not used in the computation of the plasma size, the total plasma emission, and the plasma lifetime.

5.2.2. Plasma emission

The total emission of each plasma image was computed from the sum over all pixels and normalized with the gate time used for the corresponding time step. Afterwards, the total emission was normalized to the global peak emission of all measurements, including all samples, laser energies and atmospheric conditions. Since the gain was kept constant throughout all measurements, the emission values N_{ph} are comparable to each other. It should be noted that N_{ph} does not represent the number of photons emitted from the plasma, but rather the number of photons detected by the sensor. The spectral response of the instrument can be found in Vogt (2020).

5.2.3. Plasma lifetime

Here, we define the lifetime of the plasma as the time that contains 90 % of the detected plasma emission. This definition emphasizes differences between the overall shape of the plasma emission curve and disregards effects from the absolute value of the detected plasma emission. To compute the lifetime, the data was linearly interpolated and the time when the emission reaches $0.9 \int_{t_0}^{t_{end}} N_{ph,tot}\, dt$ was used as the lifetime. It should be noted that emission from lines of interest for geochemical analysis may be observed at longer delay times than the lifetime computed in such a way.

5.2.4. Outlier detection

Some of the plasma images recorded at terrestrial atmospheric conditions show irregular plasma shapes that we identified manually to flag them as outliers. We defined outliers as images that show more than one plasma, as well as images where the plasma is unusually far from the sample. The identified images were not used in the further analysis. Plasma images identified as outliers are shown as grayed out images, and the corresponding analysis data are marked with unfilled circles or squares. We want to point out that some unmarked measurements at terrestrial conditions may fall into the outlier category but could not be discerned. In these cases, however, most of the laser energy will contribute to the plasma's internal energy and consequently to the emission and size of the plasma that are investigated in this work.

It was observed that the number of outliers in the measurements depends on the laser energy and also the lithology. Outliers were only observed at terrestrial atmospheric pressure, and higher laser energy and softer samples led to outliers occurring more frequently as can be seen in Fig. 6. To investigate if this behavior could result from a debris cloud above the sample, we decreased the laser repetition rate from the nominal rate of 2 Hz to approximately 0.1 Hz, but did not detect a change in the number of outliers. While a possible explanation of this behavior could include strong laser absorption and subsequent breakdown of the atmosphere above the sample surface, in such a scenario no dependence on the sample properties would be expected, except for optical properties. We observed a secondary plasma at distances of up to about 3 mm, where the laser irradiance is significantly reduced due to lack of focusing. Additionally, we would expect optical effects to result in a stable occurrence of an additional plasma.

Due to the dependence on the sample material and since the two regolith samples that exhibit the most outliers contain particles with a diameter of less than 1 µm, we explain this observation with plasma ignition on particles of a long-lived cloud of very fine debris that does not substantially fade within 10 s. This is also in agreement with the observation of increased outliers on soapstone, as LHS-1 and LMS-1 were measured first, followed by soapstone and basalt in the end. At Martian and airless atmospheric conditions, the thin atmosphere likely led to a sparse cloud of debris that settled faster so that no outliers were observed.

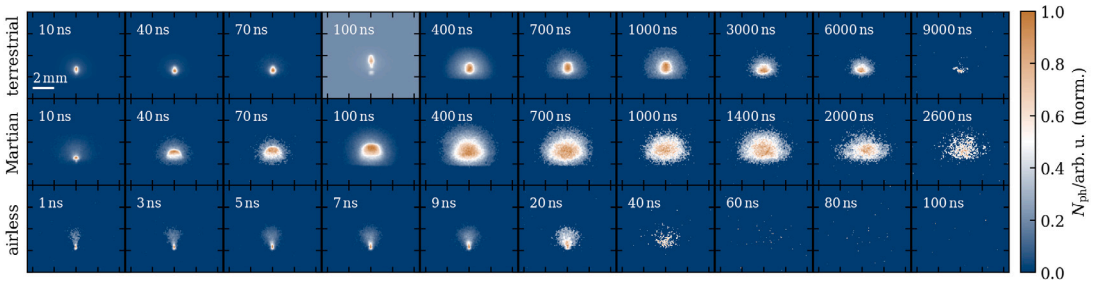

Fig. 7. Normalized plasma images of basalt with the medium laser irradiance of 1.05 GW/mm^2 at different atmospheric conditions. The detected outlier is marked with a lighter color. Note the different time scales of the measurements performed at different atmospheric conditions, see Fig. 4. The first plasma images at airless conditions are recorded within the duration of the laser pulse of 8.1 ns.

6. Results and discussion

6.1. Time series of plasma images

In the following, we show a selection of plasma image time series from which the plasma emission, lifetime and size were computed. The selection covers one set of measurements for different atmospheric conditions, different samples and different laser irradiances. Corresponding plots were generated for the complete data set and are available in the supplementary material. Each plasma image in the time series was normalized to their respective maximum, so that the entire evolution of the plasma can be viewed easily and the plasma size defined by the $FWHM_h$ can be read directly from the plots.

6.1.1. Influence of atmosphere

Fig. 7 shows plasma images from the basalt sample at the medium irradiance of 1.05 GW/mm^2 for terrestrial, Martian and airless conditions. As in all following plasma image plots, the times of the gate delay t_g are noted in the top left corner of each plasma image. Note the difference in timings for the different atmospheres that are also illustrated in Fig. 4. With the applied measurement settings, a well-defined plasma signal could be detected up to about 8 µs for terrestrial conditions, 2.8 µs for Martian conditions and 40 ns for airless conditions. The plasma image recorded at 100 ns in terrestrial atmosphere shows two plasma plumes and was thus marked as an outlier. At terrestrial atmospheric conditions, the plasma expands to a maximum of about 1.3 mm parallel to the sample surface that is reached about 3 µs after plasma ignition. Afterwards, the plasma emission remains stationary, becomes increasingly more diffuse and decays. At Martian atmospheric conditions, the plasma expands faster and reaches a larger extent of about 2.7 mm after about 400 ns due to the lower ambient pressure, followed by the decay of the plasma plume.

The plasma expands even faster at airless conditions and reaches its maximum extent of about 2.0 mm after about 40 ns. In the images, two zones of plasma emission can be distinguished. Close to the sample surface, a bright plume that is elongated normal to the sample surface can be identified. Further from the sample surface, a larger region of weak emission can be seen that shows the typical cone shape of LIPs in vacuum (Singh et al., 1990; Lasue et al., 2012). The vertical extent of the plasma remains relatively unchanged throughout the measurement.

6.1.2. Influence of lithology

In Fig. 8, the time series of plasma images at airless conditions and the highest irradiance of 1.43 GW/mm^2 are shown for all four samples. With the exception of the soapstone time series, all measurements show the elongated plasma core above the sample surface and the typical cone shaped plasma plume until about 20 ns, when the plasma shape becomes more diffuse. In case of the soapstone sample, no cone is visible and the shape of the plasma core is close to spherical. As explained above, the cone is a result of the plasma expansion velocity being higher in directions where the plasma dimensions are small and, consequently, an initially spherical plasma would not develop such a cone structure. The spherical shape of the plasma could be a result of a high evaporation and ablation rate, leading to the fast generation of a relatively large crater that supports plasma confinement, as opposed to a thin plasma layer above the sample surface. This in turn can affect the angular velocity distribution of the plume material and lead to a less directed plasma expansion. The ablation rate of a material was shown to depend on the material's hardness and consequently, a high ablation rate can be expected for soapstone, which consists mostly of talc and is thus very soft (Chide et al., 2019).

A notable difference between the samples is the onset of the plasma signal in the time series. For LHS-1, the plasma plume is first visible at 5 ns, for LMS-1 at 3 ns and for basalt and soapstone, the plume is visible in the first plasma images recorded with a gate delay of 0 ns. Considering all our measurements at airless conditions that can be accessed through the supplementary material, the first signal from the plasma plume appears within the first 7 ns. Note that the duration of the laser pulse is 8.1 ns, so that the laser pulse is still irradiating the sample at the delayed plasma onset for LHS-1 and LMS-1. Due to the lack of statistical data on each image and the fact that the temporal resolution is quite low with 2 ns for these small time steps, the exact timings should be interpreted with caution. However, in our additional data available in the supplementary materials, we see a delayed onset of the plasma signal only for the two pellet targets LHS-1 and LMS-1. At Martian and terrestrial atmospheric conditions, we used larger time steps for our measurements so that this effect can only be assessed from the first frame at 0 ns where some measurements from the LHS-1 and LMS-1 samples also lack a plasma plume signal.

Such behavior can be explained by low absorption in the sample, by high heat dissipation, by a high melting point, or by a combination of the above, so that the energy necessary to evaporate a sufficient amount of material for plasma generation is only available after prolonged irradiation of the sample. Not all of the LHS-1 measurements show a delayed plasma ignition, which can be explained by inhomogeneities in the sample makeup on the scale of the laser spot size or larger, see Fig. 3.

6.1.3. Influence of irradiance

In Fig. 9, the influence of varying the laser irradiance can be seen exemplary for the basalt sample at Martian atmospheric conditions. Within the covered irradiance range of 0.79 GW/mm^2 to 1.43 GW/mm^2, the impact on the plasma dynamics is relatively small. Apart from the drag model, previous studies used an explosion model to approximate the plasma's leading edge position as a function of time (Vogt et al., 2022; Harilal et al., 2003). This model predicts a weak dependence for the plasma radius on the explosion energy with $\propto E^{\frac{1}{5}}$. Assuming the validity of this model for intermediate times as seen in Vogt et al. (2022) and that a constant fraction of the irradiance contributes to the explosion energy, an increase of $\left(\frac{1.43\,\mathrm{GW/mm^2}}{0.79\,\mathrm{GW/mm^2}}\right)^{\frac{1}{5}} \approx 1.13$ can be expected. Considering the vertical distances from the plasma front to the sample surface, defined again by the half maximum value, at 100 ns of about

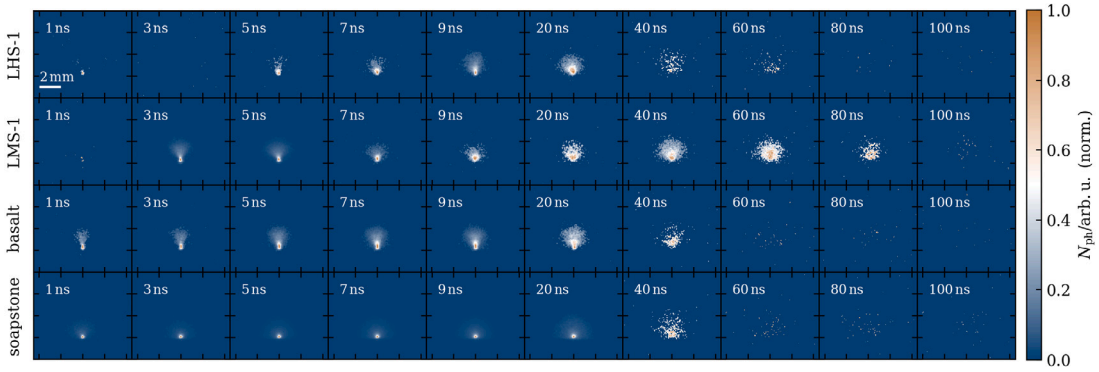

Fig. 8. Normalized plasma images of all samples at airless conditions and the highest irradiance used, 1.43 GW/mm^2. The first frames of the images are recorded within the duration of the laser pulse of 8.1 ns. For LHS-1 and LMS-1, the onset of a visible plasma signal is delayed. With the exception of soapstone, all plasma images show the typical cone shaped region of weak emission and a bright central region close to the sample surface.

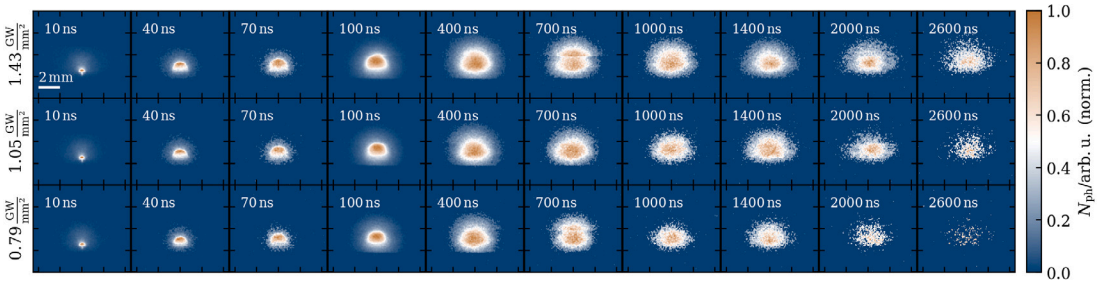

Fig. 9. Normalized plasma images of the LIP ignited from basalt at Martian atmospheric conditions for the three different investigated irradiances that correspond to laser energies of 11.86 mJ, 8.75 mJ and 6.56 mJ. Artifacts from the stitching process can be seen in the top row at 700 ns. At lower irradiances, the visible plasma plume decays earlier.

1.75 mm and 2.02 mm, respectively, the observed increase by a factor of 1.15 is reasonably close.

Apart from a change in the plasma dynamics, a lower laser irradiance leads to a shorter plasma lifetime. The stagnation size of the plasma is on average about 0.3 mm larger for the highest irradiance compared to the lowest. This is, however, within the fluctuations observed between subsequent frames.

6.2. Plasma emission, lifetime and size

The plasma emission, lifetime and size computed from the plasma images presented in the previous section are shown in Fig. 10. Measurements that were identified as outliers are also represented in the plots but marked with blank circles for the emission and blank squares for the plasma size. The plasma emission N_{ph} is marked with blue and the plasma size $FWHM_h$ with orange. The strength of the color refers to the irradiance of the measurements, with dark colors representing the highest irradiance of (1.43 ± 0.14) GW/mm^2, medium colors (1.05 ± 0.10) GW/mm^2 and light colors (0.79 ± 0.08) GW/mm^2. The lifetime of the plasma is marked with vertical lines in the color corresponding to the irradiance. The shaded areas in the plots mark the duration of the laser pulse of 8.1 ns. Each sample is represented in a separate figure, with the top panels showing measurements at terrestrial atmospheric conditions, the middle panels measurements at Martian conditions and the bottom panels at airless conditions. Note the different scales of the left axes.

6.2.1. Plasma emission

The strength of the measured plasma emission depends on the lithology, atmospheric conditions and laser irradiance. Generally, the plasma emission increases with the laser irradiance, since more energy is available for material ablation and plasma heating. This leads to higher degree of ionization and a higher electron density, which influence the continuum emission mechanisms bremsstrahlung and recombination radiation. Furthermore, the higher temperature leads to an increased population of excited atomic and ionic states and consequently a higher rate of photon emission from electronic relaxation. It should be noted that no spectral filter was applied and consequently, a significant part of the emission signal in the early evolution of the plasma can be attributed to continuum radiation (Clavé et al., 2022; Vogt et al., 2022). Previous studies using comparable experimental parameters found that for terrestrial and Martian atmospheric conditions, the continuum radiation decays by about an order of magnitude within the first 100 ns, while line emission is significantly longer-lived for the investigated wavelength range (Clavé et al., 2022; Vogt et al., 2022).

The plasma is brightest at terrestrial atmospheric conditions. At the lower atmospheric pressure of the Martian atmosphere, the plasma emission is reduced to less than about 30 % compared to terrestrial conditions. We attribute this reduction to a reduced plasma density, which leads to decreased direct heating of the plasma through plasma shielding and a more rapid temperature decrease due to a faster expansion process. At airless conditions, the plasma is even dimmer, with a reduction in emission to less than about 20 % compared to terrestrial conditions, most of which originates from the strongly emitting region close to the sample surface. This observation can be attributed to a lack of plasma confinement in addition to the effects discussed above.

The strongest plasma emission signal is obtained for soapstone at all atmospheric conditions. However, the difference in plasma brightness is most significant at early times in the plasma evolution, especially for terrestrial and Martian atmospheric conditions. For Martian atmospheric conditions, the peak emission between soapstone and basalt differs by about a factor of 2.2, while emission at 100 ns only differs by a factor of about 1.3. A significant part of the difference in initial brightness can be attributed to continuum radiation (Clavé et al., 2022; Vogt et al., 2022). As discussed in Section 6.1.2, soapstone differs from the other investigated samples, among others, by its hardness, which could lead to a more confined plasma inside the ablation crater and consequently to a hotter and brighter plasma.

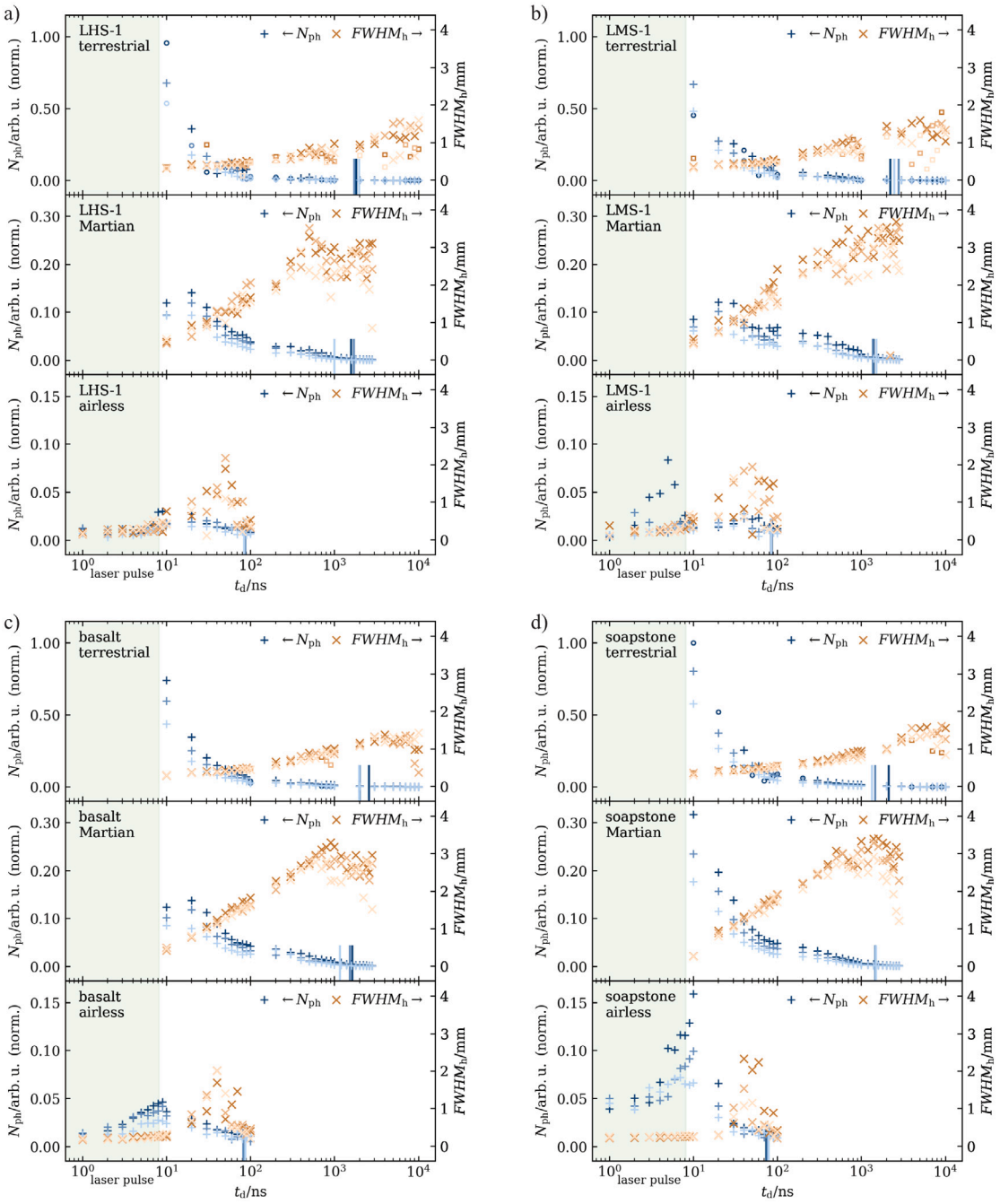

Fig. 10. Overview of all measurements analyzed in terms of their lifetime, size and emission. The left axes show the emission of the plasma plume as the sum over each plasma image divided by the corresponding gate width and the corresponding data is shown in blue. Note the different scales for the different atmospheric conditions. The right axes show the size of the plasma plume parallel to the sample surface and the corresponding data is shown in orange. Lighter color shades refer to lower laser irradiances. The duration of the laser pulse is marked as a shaded region in the left of the plots and the plasma lifetime is noted with blue bars near the time-axis. The upper, middle and lower panel for each sample show data from terrestrial, Martian and airless atmospheric conditions, respectively. (For interpretation of the references to color in this figure legend, the reader is referred to the web version of this article.)

In Fig. 11, the development of the plasma emission is shown in a double logarithmic plot exemplary for basalt with a power law of the form

$$N_{\mathrm{ph,norm}} = N^{\mathrm{max}}_{\mathrm{ph,norm}} \left(\frac{t}{\tau'}\right)^{-b} \tag{2}$$

fitted to the data points between the emission maximum and 100 ns. At 100 ns, a jump in the emission can be seen in the data of Figs. 10 and 11. Since this is the time at which the ICCD integration time was changed from 2 ns to 20 ns and this feature is present in all measurements, it can be explained by changes in the instrumentation sensitivity near the gate time limit of 2 ns. Within the fitted range, the power law shows good agreement with the data, yielding decay rates of $b_t = (1.114 \pm 0.021)$, $b_m = (0.78 \pm 0.05)$ and $b_a = (0.60 \pm 0.04)$ for terrestrial, Martian and airless conditions, respectively. Changes in the decay rate may be related to the strength of continuum emission compared to line emission at the considered times. The faster decay of continuum emission as observed in Clavé et al. (2022) may lead to a higher decay rate of the emission at terrestrial conditions where continuum emission is more prominent compared to Martian conditions. Additionally, the expansion of the plume can lead to increased emission in the case of a plume that is not optically thin, which may contribute to the slower decay of the emission in the case of Martian and airless conditions compared to terrestrial

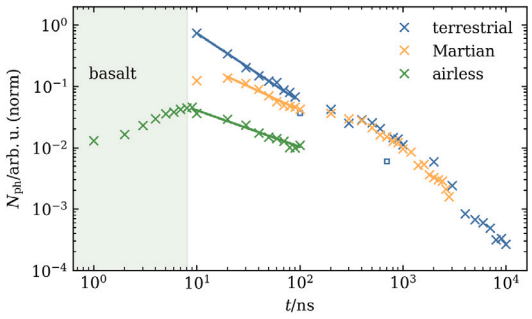

Fig. 11. Decay of the plasma emission for basalt at the high laser irradiance of 1.43 GW/mm^2. A fit of the decay with a power function results in good agreement within the fitted range. In the fits, $N^{max}_{ph,norm}$ was fixed to the maximum value of $N_{ph,norm}$. The parameters are $N^{max}_{ph,norm,t} = 0.740$, $\tau'_t = (9.98 \pm 0.12)$ ns, $b_t = (1.114 \pm 0.021)$, $N^{max}_{ph,norm,m} = 0.138$, $\tau'_m = (21.0 \pm 0.9)$ ns, $b_m = (0.78 \pm 0.05)$ and $N^{max}_{ph,norm,a} = 0.046$, $\tau'_a = (8.1 \pm 0.6)$ ns, $b_a = (0.60 \pm 0.04)$ for terrestrial, Martian and airless conditions, respectively.

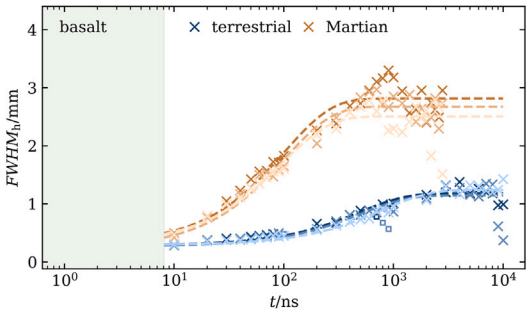

Fig. 12. The evolution of the plasma size for basalt at terrestrial and Martian atmospheric conditions can be described well by a drag model with an offset according to the plasma size at the end of the laser pulse. In this case, the offset was approximated by setting the offset value to the first data point at $t_0 = 10$ ns. The parameters for the highest irradiance data shown in dark blue and dark orange are $r_{r,t} = (0.882 \pm 0.028)$ mm, $r_{0,t} = 0.300$ mm and $\tau_t = (480 \pm 60)$ ns for terrestrial conditions and $r_{r,m} = (2.32 \pm 0.06)$ mm, $r_{0,m} = 0.50$ mm and $\tau_m = (98 \pm 12)$ ns for Martian conditions. (For interpretation of the references to color in this figure legend, the reader is referred to the web version of this article.)

conditions. While diffusion and thermal conduction may be relevant at later stages of the plasma expansion when the plume approaches its stagnation size, they can typically be disregarded in the early phase of the plasma evolution (Le et al., 2000; Zel'dovich et al., 1966). Beyond 100 ns, the slope of the decaying emission remains comparable to the fitted section, except for the noted jump at the transition to longer integration times. For terrestrial conditions, another change in the slope can be observed around 2 µs and for Martian atmospheric around 1 µs. These changes in the decay rate of the plasma emission occur roughly around the time when the plasma plume reaches its stagnation size as discussed below. At these timescales, diffusion becomes relevant and contributes to the plasma cooling and may thus explain the increased decay rate.

While the plasma emission decreases monotonously at terrestrial atmospheric conditions, for all measurements at Martian atmospheric conditions with the exception of soapstone, the emission peaks at 20 ns, well after the laser pulse has ended. We attribute this to the spectral sensitivity of our detector system. The plasma imaging system's quantum efficiency is highest around 400 nm and 600 nm (see Vogt (2020)), so that emission in this spectral region has a higher contribution to the overall plasma signal. Such an effect can be seen, for example, in Vogt et al. (2022), where the Ca I line at 422.7 nm shows a strong emission increase shortly after plasma ignition. Depending on the emitting plasma species and ambient conditions, this effect can be pronounced to varying degrees.

At airless conditions, the higher temporal resolution measurements show an increase in plasma emission for the duration of the laser pulse. The increasing emission can be explained by a combination of an increasing number of emitting species as the evaporation process continues and direct heating of the plasma vapor above the sample.

6.2.2. Plasma lifetime

While the plasmas produced from lower irradiance laser pulses are less bright as discussed above, the overall evolution does not change significantly. Since the measure of lifetime we use here considers the normalized signal, the lifetime is not affected by changes in the overall signal if the general evolution remains similar. The atmospheric conditions, however, affect the measured plasma lifetime significantly. Between terrestrial, Martian and airless atmospheric conditions, the plasma lifetime, defined here as 90% of the total emission, varies between about 3 µs, 2 µs and 80 ns, respectively. We want to stress that this lifetime reflects the measurement and computation methods discussed above, and emission lines of interest for geochemical analysis may still be observed at longer delay times than the lifetimes computed here. However, our values for Mars-like conditions in particular are in good agreement with values found in other studies, cf. Maurice et al. (2016), Schröder et al. (2019), Clavé et al. (2022), Vogt et al. (2022).

6.2.3. Plasma size

As discussed in Section 6.1.3, the influence of the laser irradiance on the plasma size is expected to be small for the range of irradiances studied in this work. Fig. 10 shows that the plasma is typically larger when ignited using a higher irradiance but the difference to the lower irradiance measurements is on the order of the data scatter. The stagnation size of the plasma changes significantly between terrestrial, Martian and airless conditions. At terrestrial atmospheric conditions, the plasma reaches a stagnation size between about 1.1 mm and 1.6 mm after between 1 µs and 3 µs, depending on the lithology and laser irradiance. Though the data scatter is significant and the influence of the lithology is small, plasmas produced from the LMS-1 and soapstone samples generally appear to be the largest at all atmospheric conditions, while plasmas produced from the basalt sample are the smallest. Due to the lower ambient pressure at Martian atmospheric conditions, the stagnation size is much larger with sizes between about 2.6 mm and 3.6 mm after between about 500 ns and 700 ns. The free expansion the plasma undergoes at airless conditions means that it does not reach a stagnation size. Instead, the plasma size peaks between around 40 ns and 50 ns after plasma ignition with sizes between 1.6 mm and 2.3 mm. This size is reached after the strongly emitting region near the sample surface has decayed after the end of the laser pulse. Due to the normalizing procedure used in our computations, the weakly emitting area becomes significant in our computations of the plasma size after the strongly emitting region vanishes.

Fig. 12 shows a fit of the drag model exemplary for basalt, which has the most stable plasma expansion as the LIP is generated from a relatively homogeneous sample. For the duration of the laser pulse, the expansion of the plasma is supported by the continued deposition of energy through laser radiation. To approximate this process, the fitted model was adapted and the two constants t_0 and r_0 were introduced that were not fitted, but determined by the time and $FWHM_h$ of the first data point after the laser pulse so that $t_0 = 10$ ns and $r_0 = FWHM_h(t_0)$.

$$r(t) = r_r(1 - e^{-\frac{t-t_0}{\tau}}) + r_0 \quad (3)$$

The fitted model shows good agreement with the data. As the plasma approaches its stagnation size $r_r + r_0$ and diffusion becomes dominant, the scatter in the data leads to some discrepancy with the fit model. For the data recorded at Martian atmospheric conditions, the fitted stagnation size decreases with the laser irradiance as expected. For the data recorded at terrestrial atmosphere, the order is reversed, although close together and consequently well explained as an artifact

of noisy data. The characteristic time scales determined from the fit in Fig. 12 are $\tau_t = (480 \pm 60)$ ns and $\tau_m = (98 \pm 12)$ ns for terrestrial and Martian atmospheric conditions, respectively.

Similarly to the time scales of expansion, the plasma lifetime is longer for terrestrial atmospheric conditions with about 2.6 µs compared to Martian atmospheric conditions with about 1.6 µs for the highest irradiance measurements on basalt. In addition to direct heating through plasma shielding, the higher ambient pressure leads to a more compact plasma with higher energy density and slower diffusion compared to a plasma with the same temperature at lower pressures, thus leading to longer emission from the plasma plume and a longer characteristic times scale.

7. Summary and conclusion

In the presented measurements, we investigated the influence that important experimental parameters have on LIBS measurements in applications for solar system exploration. For this, we acquired a data set that covers four different samples, three atmospheric conditions and three laser energies that are comparable to parameters typically found in LIBS space instrumentation. The data was acquired in such a way that enables a direct comparison of all measurements. All experimental parameters were analyzed in terms of their influence on the plasma lifetime, size and emission.

Depending on the lithology and laser irradiance, we found that plasmas ignited in terrestrial atmospheric conditions reach their stagnation size of about 1.1 mm to 1.6 mm after between 1 µs and 3 µs. At Martian atmospheric conditions, the stagnation size of 2.6 mm to 3.6 mm is reached earlier after about 500 ns to 700 ns and the plasma emission is reduced to less than about 30 % compared to terrestrial conditions. Plasmas ignited in airless conditions show, with the exception of soapstone, the typical cone of weak emission with a bright elongated area near the sample surface for the duration of the laser pulse. Afterwards, the plasma reaches its maximum extent of about 2.0 mm after 40 ns. For airless conditions, the plasma emission peaks at less than 20 % compared to terrestrial conditions and the peak occurs immediately after the laser pulse has ended.

The influence of the investigated lithologies on the plasma size and emission at terrestrial and Martian conditions is small. At airless conditions, the plasma ignited on soapstone shows about double the emission compared to all other samples. Together with the spherical shape in contrast to a cone shaped plasma, this observation may be explained by plasma confinement in a crater that leads to efficient plasma heating.

The plasma emission was observed to increase with higher laser irradiances, while the influence of the irradiance on the plasma size is small within the investigated range.

The presented data show how the laser irradiance, atmospheric conditions and sample properties influence the evolution of the plasma emission and size, and can help to constrain the requirements for future LIBS instruments.

CRediT authorship contribution statement

Fabian Seel: Writing – review & editing, Writing – original draft, Visualization, Methodology, Investigation, Formal analysis, Data curation, Conceptualization. **Susanne Schröder:** Writing – review & editing, Resources, Methodology, Funding acquisition. **Elise Clavé:** Writing – review & editing, Investigation. **Enrico Dietz:** Writing – review & editing, Investigation. **Peder Bagge Hansen:** Writing – review & editing. **Kristin Rammelkamp:** Writing – review & editing. **Heinz-Wilhelm Hübers:** Writing – review & editing, Funding acquisition.

Declaration of competing interest

The authors declare the following financial interests/personal relationships which may be considered as potential competing interests: Some of the suggested reviewers are part of the SuperCam or ChemCam team, together with some of the co-authors (Susanne Schröder, Elise Clavé, Kristn Rammelkamp and Fabian Seel).

Acknowledgment

This work was funded by the German Aerospace Center DLR.

Appendix A. Supplementary data

Supplementary material related to this article can be found online at https://doi.org/10.1016/j.icarus.2024.116376.

Data availability

Data will be made available on request.

References

Arnold, N., Gruber, J., Heitz, J., 1999. Spherical expansion of the vapor plume into ambient gas: an analytical model:. Appl. Phys. A 69 (S1), S87–S93. http://dx.doi.org/10.1007/s003399900183, http://link.springer.com/10.1007/s003399900183.

Arp, Z.A., Cremers, D.A., Harris, R.D., Oschwald, D.M., Parker, G.R., Wayne, D.M., 2004. Feasibility of generating a useful laser-induced breakdown spectroscopy plasma on rocks at high pressure: preliminary study for a Venus mission. Spectrochim. Acta Part B: Atomic Spectrosc. 59 (7), 987–999. http://dx.doi.org/10.1016/j.sab.2004.05.004, URL https://linkinghub.elsevier.com/retrieve/pii/S0584854704001211.

Autrique, D., Alexiades, V., 2014. Comment on "Laser ablation of Cu and plume expansion into 1 atm ambient gas" [j. Appl. Phys. 97, 063305 (2005)]. J. Appl. Phys. 115 (16), 166101. http://dx.doi.org/10.1063/1.4872325, URL https://pubs.aip.org/jap/article/115/16/166101/372766/Comment-on-Laser-ablation-of-Cu-and-plume.

Autrique, D., Alexiades, V., Khanal, H., 2013a. Hydrodynamic Modeling of ns-Laser Ablation. In: Ninth MSU-UAB Conference on Differential Equations and Computational Simulations, Electronic Journal of Differential Equations, Conference 20.

Autrique, D., Gornushkin, I., Alexiades, V., Chen, Z., Bogaerts, A., Rethfeld, B., 2013b. Revisiting the interplay between ablation, collisional, and radiative processes during ns-laser ablation. Appl. Phys. Lett. 103 (17), 174102. http://dx.doi.org/10.1063/1.4826505, URL https://pubs.aip.org/apl/article/103/17/174102/26468/Revisiting-the-interplay-between-ablation.

Bäuerle, D., 2000. Laser Processing and Chemistry. In: Advanced Texts in Physics, Springer Berlin Heidelberg, Berlin, Heidelberg, http://dx.doi.org/10.1007/978-3-662-04074-4, URL http://link.springer.com/10.1007/978-3-662-04074-4.

Bogaerts, A., Chen, Z., Gijbels, R., Vertes, A., 2003. Laser ablation for analytical sampling: what can we learn from modeling? Spectrochim. Acta Part B: Atomic Spectrosc. 58 (11), 1867–1893. http://dx.doi.org/10.1016/j.sab.2003.08.004, URL https://linkinghub.elsevier.com/retrieve/pii/S0584854703001666.

Brennetot, R., Lacour, J.L., Vors, E., Rivoallan, A., Vailhen, D., Maurice, S., 2003. Mars Analysis by Laser-Induced Breakdown Spectroscopy (MALIS): Influence of Mars atmosphere on plasma emission and study of factors influencing plasma emission with the use of doehlert designs. Appl. Spectrosc. 57 (7), 744–752. http://dx.doi.org/10.1366/000370203322102816, URL http://journals.sagepub.com/doi/10.1366/000370203322102816.

Carpenter, J., Fisackerly, R., De Rosa, D., Houdou, B., 2012. Scientific preparations for lunar exploration with the European lunar lander. Planet. Space Sci. 74 (1), 208–223. http://dx.doi.org/10.1016/j.pss.2012.07.024, URL https://linkinghub.elsevier.com/retrieve/pii/S0032063312002310.

Caruso, A., Gratton, R., 1968. Some properties of the plasmas produced by irradiating light solids by laser pulses. Plasma Phys. 10 (9), 867–877. http://dx.doi.org/10.1088/0032-1028/10/9/307, URL https://iopscience.iop.org/article/10.1088/0032-1028/10/9/307.

Chide, B., Maurice, S., Murdoch, N., Lasue, J., Bousquet, B., Jacob, X., Cousin, A., Forni, O., Gasnault, O., Meslin, P.-Y., Fronton, J.-F., Bassas-Portús, M., Cadu, A., Sournac, A., Mimoun, D., Wiens, R.C., 2019. Listening to laser sparks: a link between Laser-Induced Breakdown Spectroscopy, acoustic measurements and crater morphology. Spectrochim. Acta Part B: Atomic Spectrosc. 153, 50–60. http://dx.doi.org/10.1016/j.sab.2019.01.008, URL https://linkinghub.elsevier.com/retrieve/pii/S0584854718305081.

Clavé, E., Vogt, D., Schröder, S., Maurice, S., Bousquet, B., 2022. Plasma-induced luminescence spectroscopy in Martian atmospheric conditions. Spectrochim. Acta Part B: Atomic Spectrosc. 194, 106464. http://dx.doi.org/10.1016/j.sab.2022.106464, URL https://linkinghub.elsevier.com/retrieve/pii/S0584854722001082.

Cremers, D.A., Radziemski, L.J., 2013. Handbook of laser-induced breakdown spectroscopy, second ed. Wiley, A John Wiley & Sons, Ltd, Publication, Chichester, West Sussex.

Dyer, P.E., Issa, A., Key, P.H., 1990. Dynamics of excimer laser ablation of superconductors in an oxygen environment. Appl. Phys. Lett. 57 (2), 186–188. http://dx.doi.org/10.1063/1.103979, URL https://pubs.aip.org/apl/article/57/2/186/57629/Dynamics-of-excimer-laser-ablation-of.

Ennio-Smith, K., 2022. The VIPER mission, a resource-mapping mission on another celestial body. URL https://ntrs.nasa.gov/citations/20220005327.

Farid, N., Harilal, S.S., Ding, H., Hassanein, A., 2013. Dynamics of ultrafast laser plasma expansion in the presence of an ambient. Appl. Phys. Lett. 103 (19), 191112. http://dx.doi.org/10.1063/1.4829487, URL https://pubs.aip.org/apl/article/103/19/191112/129863/Dynamics-of-ultrafast-laser-plasma-expansion-in.

Fisher, B.T., Johnsen, H.A., Buckley, S.G., Hahn, D.W., 2001. Temporal gating for the optimization of laser-induced breakdown spectroscopy detection and analysis of toxic metals. Appl. Spectrosc. 55 (10), 1312–1319.

Geohegan, B., 1992. Physics and diagnostics of laser ablation plume propagation for high-t, superconductor film growth. Thin Solid Films (220), 138–145. http://dx.doi.org/10.1016/0040-6090(92)90562-P.

Gonzalo, J., Afonso, C.N., Madariaga, I., 1997. Expansion dynamics of the plasma produced by laser ablation of BaTiO3 in a gas environment. J. Appl. Phys. 81 (2), 951–955. http://dx.doi.org/10.1063/1.364188, URL https://pubs.aip.org/jap/article/81/2/951/2472/Expansion-dynamics-of-the-plasma-produced-by-laser.

Gornushkin, I., Kazakov, A., Omenetto, N., Smith, B., Winefordner, J., 2005. Experimental verification of a radiative model of laser-induced plasma expanding into vacuum. Spectrochim. Acta Part B: Atomic Spectrosc. 60 (2), 215–230. http://dx.doi.org/10.1016/j.sab.2004.11.009, URL https://linkinghub.elsevier.com/retrieve/pii/S0584854704003155.

Harilal, S.S., Bindhu, C.V., Tillack, M.S., Najmabadi, F., Gaeris, A.C., 2003. Internal structure and expansion dynamics of laser ablation plumes into ambient gases. J. Appl. Phys. 93 (5), 2380–2388. http://dx.doi.org/10.1063/1.1544070, URL http://aip.scitation.org/doi/10.1063/1.1544070.

Harilal, S.S., Miloshevsky, G.V., Diwakar, P.K., LaHaye, N.L., Hassanein, A., 2012. Experimental and computational study of complex shockwave dynamics in laser ablation plumes in argon atmosphere. Phys. Plasmas 19 (8), 083504. http://dx.doi.org/10.1063/1.4745867, URL http://aip.scitation.org/doi/10.1063/1.4745867.

Harilal, S.S., Sizyuk, T., Hassanein, A., Campos, D., Hough, P., Sizyuk, V., 2011. The effect of excitation wavelength on dynamics of laser-produced tin plasma. J. Appl. Phys. 109 (6), 063306. http://dx.doi.org/10.1063/1.3562143, URL https://pubs.aip.org/jap/article/109/6/063306/988349/The-effect-of-excitation-wavelength-on-dynamics-of.

Harri, A.-M., Paton, M., Hieta, M., Polkko, J., Newman, C., Pla-Garcia, J., Leino, J., Mäkinen, T., Kauhanen, J., Jaakonaho, I., Sánchez-Lavega, A., Hueso, R., Genzer, M., Lorenz, R., Lemmon, M., Vicente-Retortillo, A., Tamppari, L.K., Viudez-Moreiras, D., Torre-Juarez, M.D.L., Savijärvi, H., Rodríguez-Manfredi, J.A., Martinez, G., 2024. Perseverance MEDA atmospheric pressure observations—Initial results. J. Geophys. Res. Planets 129 (3), e2023JE007880. http://dx.doi.org/10.1029/2023JE007880, URL https://agupubs.onlinelibrary.wiley.com/doi/10.1029/2023JE007880.

Harris, C.R., Millman, K.J., Van Der Walt, S.J., Gommers, R., Virtanen, P., Cournapeau, D., Wieser, E., Taylor, J., Berg, S., Smith, N.J., Kern, R., Picus, M., Hoyer, S., Van Kerkwijk, M.H., Brett, M., Haldane, A., Del Río, J.F., Wiebe, M., Peterson, P., Gérard-Marchant, P., Sheppard, K., Reddy, T., Weckesser, W., Abbasi, H., Gohlke, C., Oliphant, T.E., 2020. Array programming with NumPy. Nature 585 (7825), 357–362. http://dx.doi.org/10.1038/s41586-020-2649-2, URL https://www.nature.com/articles/s41586-020-2649-2.

Heiken, G.H., Vaniman, D.T., French, B.M., 1991. Lunar Sourcebook, A User's Guide to the Moon. Publication Title: Lunar Sourcebook, A User's Guide to the Moon ADS Bibcode: 1991lsug.book.....H, URL https://ui.adsabs.harvard.edu/abs/1991lsug.book.....H.

Hermann, J., Axente, E., Craciun, V., Taleb, A., Pelascini, F., 2018. Evaluation of pressure in a plasma produced by laser ablation of steel. Spectrochim. Acta Part B: Atomic Spectrosc. 143, 63–70. http://dx.doi.org/10.1016/j.sab.2018.02.015, URL https://linkinghub.elsevier.com/retrieve/pii/S058485471730616X.

Itina, T.E., Hermann, J., Delaporte, P., Sentis, M., 2002. Laser-generated plasma plume expansion: Combined continuous-microscopic modeling. Phys. Rev. E 66 (6), 066406. http://dx.doi.org/10.1103/PhysRevE.66.066406, URL https://link.aps.org/doi/10.1103/PhysRevE.66.066406.

Kane, K.Y., Cremers, D.A., 1992a. An in situ technique for elemental analysis of lunar surfaces. New Technol. Lunar Resour. Assessment 34–35.

Kane, K.Y., Cremers, D.A., 1992b. Remote elemental analysis of planetary surfaces using laser-induced breakdown spectroscopy. Lunar and Planet. Sci. Conf. 23, 651–652.

Keldysh, L.V., 2023. Ionization in the field of a strong electromagnetic wave. In: Selected Papers of Leonid V Keldysh. WORLD SCIENTIFIC, pp. 56–63. http://dx.doi.org/10.1142/9789811279461_0008, URL https://www.worldscientific.com/doi/10.1142/9789811279461_0008.

Knight, A.K., Scherbarth, N.L., Cremers, D.A., Ferris, M.J., 2000. Characterization of laser-induced breakdown spectroscopy (LIBS) for application to space exploration. Appl. Spectrosc. 54 (3), 331–340. http://dx.doi.org/10.1366/0003702001949591, URL http://journals.sagepub.com/doi/10.1366/0003702001949591.

Krokhin, O.N., 1965. Self-regulating regime of plasma heating by laser radiation. Z. Ang. Math. Phys. ZAMP 16 (1), 123–124. http://dx.doi.org/10.1007/BF01589073, URL http://link.springer.com/10.1007/BF01589073.

Lasue, J., Wiens, R.C., Clegg, S.M., Vaniman, D.T., Joy, K.H., Humphries, S., Mezzacappa, A., Melikechi, N., McInroy, R.E., Bender, S., 2012. Remote laser-induced breakdown spectroscopy (LIBS) for lunar exploration. J. Geophys. Res. Planets 117 (E1), 2011JE003898. http://dx.doi.org/10.1029/2011JE003898, URL https://agupubs.onlinelibrary.wiley.com/doi/10.1029/2011JE003898.

Laxmiprasad, A.S., Sridhar, R.V.L.N., Goswami, A., Lohar, K.A., Rao, M.V.H., Shila, K.V., Mahajan, M., Raha, B., Smaran, T.S., Krishnamprasad, B., 2020. Laser induced breakdown spectroscope on chandrayaan-2 Rover:A Miniaturized Mid-UV to visible active spectrometer for lunar surface chemistry studies. Current Sci. 118 (4), 573. http://dx.doi.org/10.18520/cs/v118/i4/573-581, URL https://www.currentscience.ac.in/Volumes/118/04/0573.pdf.

Le, H.C., Zeitoun, D.E., Parisse, J.D., Sentis, M., Marine, W., 2000. Modeling of gas dynamics for a laser-generated plasma: Propagation into low-pressure gases. Phys. Rev. E 62 (3), 4152–4161. http://dx.doi.org/10.1103/PhysRevE.62.4152, URL https://link.aps.org/doi/10.1103/PhysRevE.62.4152.

Liu, H., Ashfold, M.N.R., Meehan, D.N., Wagenaars, E., 2019. Wavelength-dependent variations of the electron characteristics in laser-induced plasmas: A combined hydrodynamic and adiabatic expansion modelling and time-gated, optical emission imaging study. J. Appl. Phys. 125 (8), 083304. http://dx.doi.org/10.1063/1.5052392, URL https://pubs.aip.org/jap/article/125/8/083304/133717/Wavelength-dependent-variations-of-the-electron.

Lorenz, R.D., Turtle, E.P., Barnes, J.W., Trainer, M.G., 2018. Dragonfly: A rotorcraft lander concept for scientific exploration at titan. Johns Hopkins APL Tech. Dig. 34 (3).

Mao, X., Russo, R.E., 1996. Invited paper Observation of plasma shielding by measuring transmitted and reflected laser pulse temporal profiles. Appl. Phys. A 64 (1), 1–6. http://dx.doi.org/10.1007/s003390050437, URL http://link.springer.com/10.1007/s003390050437.

Maurice, S., Clegg, S.M., Wiens, R.C., Gasnault, O., Rapin, W., Forni, O., Cousin, A., Sautter, V., Mangold, N., Le Deit, L., Nachon, M., Anderson, R.B., Lanza, N.L., Fabre, C., Payré, V., Lasue, J., Meslin, P.-Y., Léveillé, R.J., Barraclough, B.L., Beck, P., Bender, S.C., Berger, G., Bridges, J.C., Bridges, N.T., Dromart, G., Dyar, M.D., Francis, R., Frydenvang, J., Gondet, B., Ehlmann, B.L., Herkenhoff, K.E., Johnson, J.R., Langevin, Y., Madsen, M.B., Melikechi, N., Lacour, J.-L., Le Mouélic, S., Lewin, E., Newsom, H.E., Ollila, A.M., Pinet, P., Schröder, S., Sirven, J.-B., Tokar, R.L., Toplis, M.J., d'Uston, C., Vaniman, D.T., Vasavada, A.R., 2016. ChemCam activities and discoveries during the nominal mission of the Mars Science Laboratory in gale crater, Mars. J. Anal. At. Spectrom. 31 (4), 863–889. http://dx.doi.org/10.1039/C5JA00417A, URL http://xlink.rsc.org/?DOI=C5JA00417A.

Maurice, S., Wiens, R.C., Bernardi, P., Caï s, P., Robinson, S., Nelson, T., Gasnault, O., Reess, J.-M., Deleuze, M., Rull, F., Manrique, J.-A., Abbaki, S., Anderson, R.B., André, Y., Angel, S.M., Arana, G., Battault, T., Beck, P., Benzerara, K., Bernard, S., Berthias, J.-P., Beyssac, O., Bonafous, M., Bousquet, B., Boutillier, M., Cadu, A., Castro, K., Chapron, F., Chide, B., Clark, K., Clavé, E., Clegg, S., Cloutis, E., Collin, C., Cordoba, E.C., Cousin, A., Dameury, J.-C., D'Anna, W., Daydou, Y., Debus, A., Deflores, L., Dehouck, E., Delapp, D., De Los Santos, G., Donny, C., Doressoundiram, A., Dromart, G., Dubois, B., Dufour, A., Dupieux, M., Egan, M., Ervin, J., Fabre, C., Fau, A., Fischer, W., Forni, O., Fouchet, T., Frydenvang, J., Gauffre, S., Gauthier, M., Gharakanian, V., Gilard, O., Gontijo, I., Gonzalez, R., Granena, D., Grotzinger, J., Hassen-Khodja, R., Heim, M., Hello, Y., Hervet, G., Humeau, O., Jacob, X., Jacquinod, S., Johnson, J.R., Kouach, D., Lacombe, G., Lanza, N., Lapauw, L., Laserna, J., Lasue, J., Le Deit, L., Le Mouélic, S., Le Comte, E., Lee, Q.-M., Legett, C., Leveille, R., Lewin, E., Leyrat, C., Lopez-Reyes, G., Lorenz, R., Lucero, B., Madariaga, J.M., Madsen, S., Madsen, M., Mangold, N., Manni, F., Mariscal, J.-F., Martinez-Frias, J., Mathieu, K., Mathon, R., McCabe, K.P., McConnochie, T., McLennan, S.M., Mekki, J., Melikechi, N., Meslin, P.-Y., Micheau, Y., Michel, Y., Michel, J.M., Mimoun, D., Misra, A., Montagnac, G., Montaron, C., Montmessin, F., Moros, J., Mousset, V., Morizet, Y., Murdoch, N., Newell, R.T., Newsom, H., Nguyen Tuong, N., Ollila, A.M., Orttner, G., Oudda, L., Pares, L., Parisot, J., Parot, Y., Pérez, R., Pheav, D., Picot, L., Pilleri, P., Pilorget, C., Pinet, P., Pont, G., Poulet, F., Quantin-Nataf, C., Quertier, B., Rambaud, D., Rapin, W., Romano, P., Roucayrol, L., Royer, C., Ruellan, M., Sandoval, B.F., Sautter, V., Schoppers, M.J., Schröder, S., Seran, H.-C., Sharma, S.K., Sobron, P., Sodki, M., Sournac, A., Sridhar, V., Standarovsky, D., Storms, S., Striebig, N., Tatat, M., Toplis, M., Torre-Fdez, I., Toulemont, N., Velasco, C., Veneranda, M., Venhaus, D., Virmontois, C., Viso, M., Willis, P., Wong, K.W., 2021. The SuperCam instrument suite on the Mars 2020 rover: Science objectives and mast-unit description. Space Sci. Rev. 217 (3), 47. http://dx.doi.org/10.1007/s11214-021-00807-w, URL https://link.springer.com/10.1007/s11214-021-00807-w.

Maurice, S., Wiens, R.C., Saccoccio, M., Barraclough, B., Gasnault, O., Forni, O., Mangold, N., Baratoux, D., Bender, S., Berger, G., Bernardin, J., Berthé, M., Bridges, N., Blaney, D., Bouyé, M., Caï s, P., Clark, B., Clegg, S., Cousin, A.,

Cremers, D., Cros, A., DeFlores, L., Derycke, C., Dingler, B., Dromart, G., Dubois, B., Dupieux, M., Durand, E., d'Uston, L., Fabre, C., Faure, B., Gaboriaud, A., Gharsa, T., Herkenhoff, K., Kan, E., Kirkland, L., Kouach, D., Lacour, J.-L., Langevin, Y., Lasue, J., Le Mouélic, S., Lescure, M., Lewin, E., Limonadi, D., Manhès, G., Mauchien, P., McKay, C., Meslin, P.-Y., Michel, Y., Miller, E., Newsom, H.E., Orttner, G., Paillet, A., Parès, L., Parot, Y., Pérez, R., Pinet, P., Poitrasson, F., Quertier, B., Sallé, B., Sotin, C., Sautter, V., Séran, H., Simmonds, J.J., Sirven, J.-B., Stiglich, R., Striebig, N., Thocaven, J.-J., Toplis, M.J., Vaniman, D., 2012. The ChemCam instrument suite on the Mars Science Laboratory (MSL) rover: Science objectives and mast unit description. Space Sci. Rev. 170 (1–4), 95–166. http://dx.doi.org/10.1007/s11214-012-9912-2, URL http://link.springer.com/10.1007/s11214-012-9912-2.

Murakami, M., Kang, Y.-G., Nishihara, K., Fujioka, S., Nishimura, H., 2005. Ion energy spectrum of expanding laser-plasma with limited mass. Phys. Plasmas 12 (6), 062706. http://dx.doi.org/10.1063/1.1928247, URL https://pubs.aip.org/pop/article/12/6/062706/762161/Ion-energy-spectrum-of-expanding-laser-plasma-with.

Noll, R., 2012. Laser-induced breakdown spectroscopy. Springer Berlin Heidelberg, URL https://doi.org/10.1007/978-3-642-20668-9_2.

Radziemski, L.J., Cremers, D.A., 1989. Laser-induced plasmas and applications.

Rammelkamp, K., Schröder, S., Lomax, B.A., Clavé, E., Hübers, H.-W., 2024. LIBS for prospecting and Raman spectroscopy for monitoring: two feasibility studies for supporting in-situ resource utilization. Front. Space Technol. 5, 1336548. http://dx.doi.org/10.3389/frspt.2024.1336548, URL https://www.frontiersin.org/articles/10.3389/frspt.2024.1336548/full.

Sallé, B., Cremers, D.A., Maurice, S., Wiens, R.C., 2005. Laser-induced breakdown spectroscopy for space exploration applications: Influence of the ambient pressure on the calibration curves prepared from soil and clay samples. Spectrochim. Acta Part B: Atomic Spectrosc. 60 (4), 479–490. http://dx.doi.org/10.1016/j.sab.2005.02.009, URL https://linkinghub.elsevier.com/retrieve/pii/S0584854705000273.

Schröder, S., Rammelkamp, K., Vogt, D., Gasnault, O., Hübers, H.-W., 2019. Contribution of a martian atmosphere to laser-induced breakdown spectroscopy (LIBS) data and testing its emission characteristics for normalization applications. Icarus 325, 1–15. http://dx.doi.org/10.1016/j.icarus.2019.02.017, URL https://linkinghub.elsevier.com/retrieve/pii/S0019103518307760.

Seel, F., Schröder, S., Vogt, D., Dietz, E., Hübers, H.-W., Gensch, M., 2023. Generation and evolution of laser-induced shock waves under Martian atmospheric conditions. Icarus 394, 115405. http://dx.doi.org/10.1016/j.icarus.2022.115405, URL https://linkinghub.elsevier.com/retrieve/pii/S0019103522004973.

Singh, R.K., Holland, O.W., Narayan, J., 1990. Theoretical model for deposition of superconducting thin films using pulsed laser evaporation technique. J. Appl. Phys. 68 (1), 233–247. http://dx.doi.org/10.1063/1.347123, URL https://pubs.aip.org/jap/article/68/1/233/175862/Theoretical-model-for-deposition-of.

Singh, R.K., Narayan, J., 1990. Pulsed-laser evaporation technique for deposition of thin films: Physics and theoretical model. Phys. Rev. B 41 (13), 8843–8859. http://dx.doi.org/10.1103/PhysRevB.41.8843, URL https://link.aps.org/doi/10.1103/PhysRevB.41.8843.

Singh, J.P., Thakur, S.N. (Eds.), 2020. Laser-induced breakdown spectroscopy, second ed. Elsevier, Amsterdam Kidlington, Oxford Cambridge, MA.

Virtanen, P., Gommers, R., Oliphant, T.E., Haberland, M., Reddy, T., Cournapeau, D., Burovski, E., Peterson, P., Weckesser, W., Bright, J., van der Walt, S.J., Brett, M., Wilson, J., Millman, K.J., Mayorov, N., Nelson, A.R.J., Jones, E., Kern, R., Larson, E., Carey, C.J., Polat, I., Feng, Y., Moore, E.W., VanderPlas, J., Laxalde, D., Perktold, J., Cimrman, R., Henriksen, I., Quintero, E.A., Harris, C.R., Archibald, A.M., Ribeiro, A.H., Pedregosa, F., van Mulbregt, P., SciPy 1.0 Contributors, Vijaykumar, A., Bardelli, A.P., Rothberg, A., Hilboll, A., Kloeckner, A., Scopatz, A., Lee, A., Rokem, A., Woods, C.N., Fulton, C., Masson, C., Häggström, C., Fitzgerald, C., Nicholson, D.A., Hagen, D.R., Pasechnik, D.V., Olivetti, E., Martin, E., Wieser, E., Silva, F., Lenders, F., Wilhelm, F., Young, G., Price, G.A., Ingold, G.-L., Allen, G.E., Lee, G.R., Audren, H., Probst, I., Dietrich, J.P., Silterra, J., Webber, J.T., Slavič, J., Nothman, J., Buchner, J., Kulick, J., Schönberger, J.L., de Miranda Cardoso, J.V., Reimer, J., Harrington, J., Rodríguez, J.L.C., Nunez-Iglesias, J., Kuczynski, J., Tritz, K., Thoma, M., Newville, M., Kümmerer, M., Bolingbroke, M., Tartre, M., Pak, M., Smith, N.J., Nowaczyk, N., Shebanov, N., Pavlyk, O., Brodtkorb, P.A., Lee, P., McGibbon, R.T., Feldbauer, R., Lewis, S., Tygier, S., Sievert, S., Vigna, S., Peterson, S., More, S., Pudlik, T., Oshima, T., Pingel, T.J., Robitaille, T.P., Spura, T., Jones, T.R., Cera, T., Leslie, T., Zito, T., Krauss, T., Upadhyay, U., Halchenko, Y.O., Vázquez-Baeza, Y., 2020. SciPy 1.0: fundamental algorithms for scientific computing in Python. Nat. Methods 17 (3), 261–272. http://dx.doi.org/10.1038/s41592-019-0686-2, URL http://www.nature.com/articles/s41592-019-0686-2.

Vogt, D.S., 2020. Laser-Induced Breakdown Spectroscopy for the Exploration of Mars: Analysis of Molecular Emissions and Spatial Characterization of the Plasma Doctoral dissertation. Humboldt-Universität zu Berlin, Berlin, URL https://elib.dlr.de/131240/.

Vogt, D., Schröder, S., Frohmann, S., Hansen, P., Seel, F., Gensch, M., Hübers, H.-W., 2022. Spatiotemporal characterization of the laser-induced plasma plume in simulated Martian conditions. Spectrochim. Acta Part B: Atomic Spectrosc. 187, 106326. http://dx.doi.org/10.1016/j.sab.2021.106326, URL https://linkinghub.elsevier.com/retrieve/pii/S0584854721002834.

Wan, X., 2021. Design, function, and implementation of China's first LIBS instrument (MarSCoDe) on the Zhurong Mars rover. At. Spectrosc. 42 (5), http://dx.doi.org/10.46770/AS.2021.608, URL http://www.at-spectrosc.com/as/article/pdf/2021608.

Wiens, R.C., Maurice, S., Barraclough, B., Saccoccio, M., Barkley, W.C., Bell, J.F., Bender, S., Bernardin, J., Blaney, D., Blank, J., Bouyé, M., Bridges, N., Bultman, N., Caï s, P., Clanton, R.C., Clark, B., Clegg, S., Cousin, A., Cremers, D., Cros, A., DeFlores, L., Delapp, D., Dingler, R., D'Uston, C., Darby Dyar, M., Elliott, T., Enemark, D., Fabre, C., Flores, M., Forni, O., Gasnault, O., Hale, T., Hays, C., Herkenhoff, K., Kan, E., Kirkland, L., Kouach, D., Landis, D., Langevin, Y., Lanza, N., LaRocca, F., Lasue, J., Latino, J., Limonadi, D., Lindensmith, C., Little, C., Mangold, N., Manhes, G., Mauchien, P., McKay, C., Miller, E., Mooney, J., Morris, R.V., Morrison, L., Nelson, T., Newsom, H., Ollila, A., Ott, M., Pares, L., Perez, R., Poitrasson, F., Provost, C., Reiter, J.W., Roberts, T., Romero, F., Sautter, V., Salazar, S., Simmonds, J.J., Stiglich, R., Storms, S., Striebig, N., Thocaven, J.-J., Trujillo, T., Ulibarri, M., Vaniman, D., Warner, N., Waterbury, R., Whitaker, R., Witt, J., Wong-Swanson, B., 2012. The ChemCam instrument suite on the Mars Science Laboratory (MSL) rover: Body unit and combined system tests. Space Sci. Rev. 170 (1–4), 167–227. http://dx.doi.org/10.1007/s11214-012-9902-4, URL http://link.springer.com/10.1007/s11214-012-9902-4.

Wiens, R.C., Maurice, S., Robinson, S.H., Nelson, A.E., Cais, P., Bernardi, P., Newell, R.T., Clegg, S., Sharma, S.K., Storms, S., Deming, J., Beckman, D., Ollila, A.M., Gasnault, O., Anderson, R.B., André, Y., Michael Angel, S., Arana, G., Auden, E., Beck, P., Becker, J., Benzerara, K., Bernard, S., Beyssac, O., Borges, L., Bousquet, B., Boyd, K., Caffrey, M., Carlson, J., Castro, K., Celis, J., Chide, B., Clark, K., Cloutis, E., Cordoba, E.C., Cousin, A., Dale, M., Deflores, L., Delapp, D., Deleuze, M., Dirmyer, M., Donny, C., Dromart, G., George Duran, M., Egan, M., Ervin, J., Fabre, C., Fau, A., Fischer, W., Forni, O., Fouchet, T., Fresquez, R., Frydenvang, J., Gasway, D., Gontijo, I., Grotzinger, J., Jacob, X., Jacquinod, S., Johnson, J.R., Klisiewicz, R.A., Lake, J., Lanza, N., Laserna, J., Lasue, J., Le Mouélic, S., Legett, C., Leveille, R., Lewin, E., Lopez-Reyes, G., Lorenz, R., Lorigny, E., Love, S.P., Lucero, B., Madariaga, J.M., Madsen, M., Madsen, S., Mangold, N., Manrique, J.A., Martinez, J.P., Martinez-Frias, J., McCabe, K.P., McConnochie, T.H., McGlown, J.M., McLennan, S.M., Melikechi, N., Meslin, P.-Y., Michel, J.M., Mimoun, D., Misra, A., Montagnac, G., Montmessin, F., Mousset, V., Murdoch, N., Newsom, H., Ott, L.A., Ousnamer, Z.R., Pares, L., Parot, Y., Pawluczyk, R., Glen Peterson, C., Pilleri, P., Pinet, P., Pont, G., Poulet, F., Provost, C., Quertier, B., Quinn, H., Rapin, W., Reess, J.-M., Regan, A.H., Reyes-Newell, A.L., Romano, P.J., Royer, C., Rull, F., Sandoval, B., Sarrao, J.H., Sautter, V., Schoppers, M.J., Schröder, S., Seitz, D., Shepherd, T., Sobron, P., Dubois, B., Sridhar, V., Toplis, M.J., Torre-Fdez, I., Trettel, I.A., Underwood, M., Valdez, A., Valdez, J., Venhaus, D., Willis, P., 2021. The SuperCam instrument suite on the NASA Mars 2020 rover: Body unit and combined system tests. Space Sci. Rev. 217 (1), 4. http://dx.doi.org/10.1007/s11214-020-00777-5, URL http://link.springer.com/10.1007/s11214-020-00777-5.

Xu, W., Liu, X., Yan, Z., Li, L., Zhang, Z., Kuang, Y., Jiang, H., Yu, H., Yang, F., Liu, C., Wang, T., Li, C., Jin, Y., Shen, J., Wang, B., Wan, W., Chen, J., Ni, S., Ruan, Y., Xu, R., Zhang, C., Yuan, Z., Wan, X., Yang, Y., Li, Z., Shen, Y., Liu, D., Wang, B., Yuan, R., Bao, T., Shu, R., 2021. The MarSCoDe instrument suite on the Mars rover of China's Tianwen-1 Mission. Space Sci. Rev. 217 (5), 64. http://dx.doi.org/10.1007/s11214-021-00836-5, URL https://link.springer.com/10.1007/s11214-021-00836-5.

Zel'dovich, J.B., Rajzer, J.P., Hayes, W.D., Probstein, R.F., 1966. Physics of shock waves and high-temperature hydrodynamic phenomena, vol. 1, Academic Press, New York.